Atmospheric
Chemistry
and Physics
Discussions

New particle formation from sulfuric acid and ammonia: nucleation and growth model based on thermodynamics derived from CLOUD measurements for a wide range of conditions

Andreas Kürten

Institute for Atmospheric and Environmental Sciences, Goethe University Frankfurt, 60438 Frankfurt am Main, Germany.

Correspondence to: Andreas Kürten (kuerten@iau.uni-frankfurt.de)

Abstract

Understanding new particle formation and growth is important because of the strong impact of these processes on climate and air quality. Measurements to elucidate the main new particle formation mechanisms are essential; however, these mechanisms have to be implemented in models to estimate their impact on the regional and global scale. Parameterizations are computationally cheap ways of implementing nucleation schemes in models but they have their limitations, as they do not necessarily include all relevant parameters. Process models using sophisticated nucleation schemes can be useful for the generation of look-up tables in large-scale models or for the analysis of individual new particle formation events. In addition, some other important properties can be derived from a process model that implicitly calculates the evolution of the full aerosol size distribution, e.g., the particle growth rates. Within this study, a model (SANTIAGO, Sulfuric acid Ammonia NucleaTIon And GrOwth model) is constructed that simulates new particle formation starting from the monomer of sulfuric acid up to a particle size of several hundred nanometers. The smallest sulfuric acid clusters containing one to four acid molecules and varying amount of base (ammonia) are allowed to evaporate in the model, whereas growth beyond the pentamer (5 sulfuric acid molecules) is assumed to be entirely collision-controlled. The main goal of the present study is to derive appropriate thermodynamic data needed to calculate the cluster evaporation rates as a function of temperature. These data are derived numerically from CLOUD (Cosmics Leaving OUtdoor Droplets) chamber new particle formation rates for neutral sulfuric acid-water-ammonia nucleation at temperatures between 208 K and 292 K. The numeric methods include an optimization scheme to derive the best estimates for the thermodynamic data (dH and dS) and a Monte Carlo method to derive their probability density functions. The derived data are compared to literature values. Using different data sets for dH and dS in SANTIAGO detailed comparison between model results and measured CLOUD new particle formation rates is discussed.

Atmospheric
Chemistry
and Physics
Discussions

1. INTRODUCTION

The formation of new aerosol particles from the gas phase (nucleation) is the most important source of cloud condensation nuclei (CCN) in the free and upper troposphere (Dunne et al., 2016; Gordon et al., 2017). Binary new particle formation (NPF) from sulfuric acid and water is thought to be an important mechanism at cold conditions that can be enhanced by ions (Lee et al., 2003; Kirkby et al., 2011; Duplissy et al., 2016). The ternary system involving ammonia besides sulfuric acid and water can yield significantly enhanced NPF rates (Ball et al., 1999; Benson et al., 2009; Glasoe et al., 2015; Kirkby et al., 2011; Kürten et al., 2016). The addition of only a few pptv of ammonia can increase NPF rates by several orders of magnitude compared with the pure binary system (Kürten et al., 2016). The importance of ammonia in terms of NPF is highlighted by recent modeling studies, where a large fraction of CCN originates from ternary H_2SO_4-H_2O-NH_3 nucleation (Dunne et al., 2016; Gordon et al., 2017). The detection of ammonia above several pptv in the upper troposphere by recent satellite measurements supports these findings (Höpfner et al., 2016). Furthermore, an aircraft campaign up to ~5 km altitude measured elevated NH_3 concentrations over Texas (Nowak et al., 2010). Therefore, it is likely that ammonia plays an important role in new particle formation in the free troposphere. An expected future increase in the anthropogenic ammonia emissions could even increase the significance of ammonia in terms of NPF (Clarisse et al., 2009).

At cold conditions, NPF from H_2SO_4-H_2O-NH_3 is efficient enough to explain NPF at atmospherically relevant concentrations of sulfuric acid and ammonia (Kirkby et al., 2011; Dunne et al., 2016; Kürten et al., 2016). However, the involvement of ammonia in the formation of new particles at the relatively warm conditions close to the surface is not clear yet. A recent study indicates that ion-induced ternary nucleation can explain some new particle formation events in the boreal forest in Finland (Yan et al., 2018); evidence that NH_3 is important in polluted boundary layer environments has been presented earlier (Chen et al., 2012). Most recently, Jokinen et al., (2018) showed that ion-induced ternary nucleation is important in coastal Antarctica. The importance of ammonia in enhancing boundary layer nucleation in the presence of highly-oxygenated molecules (HOM) from monoterpenes and sulfuric acid has recently been described (Lehtipalo et al., 2018).

In order to model nucleation, knowledge about cluster evaporation rates is required. This can either be gained by measurements in a flow tube (Hanson and Eisele, 2002; Jen et al., 2014; Jen et al., 2016; Hanson et al., 2017) or in a chamber such as CLOUD (Cosmics Leaving OUtdoor Droplets, Kürten et al., 2015a). Another possibility is to apply quantum chemical (QC) calculations (Kurtén et al., 2007; Nadykto and Yu, 2007; Ortega et al., 2012; Elm et al., 2013; Elm and Kristensen, 2017; Yu et al., 2018). Comparison between experimental data measured at the CLOUD chamber and modeled formation rates using the ACDC (Atmospheric Cluster Dynamics Code) model (McGrath et al., 2012) with evaporation rates from quantum chemistry (Ortega et al., 2012) yielded good agreement for some conditions (208 and 223 K). For higher temperatures ($\geq$ 248 K) the model generally overestimated the formation rates up to several orders of magnitude. A more recently developed nucleation model, also relying on evaporation rates from QC calculations, yields good agreement with the CLOUD data for some conditions (Yu et al., 2018).

Atmospheric
Chemistry
and Physics
Discussions

84　　　For the global modeling studies by Dunne et al. (2016) and Gordon et al. (2017) CLOUD
85　　data have been parameterized to yield nucleation rates for four different channels (binary
86　　neutral and ion-induced, and ternary neutral and ion-induced). The parameterization works well
87　　and describes the nucleation rates over a wide range of conditions (Dunne et al., 2016) but it
88　　also has its limitations. First, it does not give any insights on the stability of individual sulfuric
89　　acid-ammonia clusters. Second, the influence of other parameters on nucleation (e.g., the
90　　condensation sink) cannot be tested, while the model by Yu et al. (2018) considers the effect of
91　　the condensation sink on the nucleation rate. Third, the parameterization provides only the
92　　nucleation rate, while a full nucleation model utilizing size bins over a wide diameter range can
93　　also yield the particle growth rates (Li and McMurry, 2018).
94　　　In the present study a model covering the aerosol size distribution over a wide size range,
95　　i.e., from the monomer of sulfuric acid up to several hundred nanometers, is constructed. The
96　　model simulates acid-base nucleation and considers evaporation rates for the clusters containing
97　　one to four sulfuric acid molecules and variable number of base molecules. The model allows
98　　calculating new particle formation and growth rates at different sizes and considers sinks like
99　　wall loss, dilution and coagulation. SANTIAGO (Sulfuric acid Ammonia NucleaTIon And
100　　GrOwth model) is an extension of a previous simpler model version used to simulate acid-base
101　　nucleation involving dimethylamine (Kürten et al., 2014; Kürten et al., 2018). The model
102　　extension in the present study is a prerequisite for the main goal to derive the thermochemical
103　　parameters (dH and dS) for the sulfuric acid-ammonia system from CLOUD chamber data
104　　(Dunne et al., 2016; Kürten et al., 2016). The data cover electrically neutral conditions for the
105　　clusters up to the tetramer (containing four sulfuric acid molecules and up to four ammonia
106　　molecules). First, a model has been developed that uses molecular and geometric size bins to
107　　cover a wide particle size range (starting with the monomer of sulfuric acid). Second, two
108　　numeric algorithms yield a best fit for the dH and dS values and their probability density
109　　functions (pdf). The pdf are obtained by using a Monte Carlo method introduced by Kupiainen-
110　　Määttä (2016). In total, CLOUD data from 125 experiments are considered; these cover the
111　　range from 208 K to 292 K and a wide range of atmospherically relevant sulfuric acid and
112　　ammonia concentrations. The results of the model are compared to the measured CLOUD data
113　　and further comparison regarding the thermochemical data from literature (Ortega et al., 2012;
114　　Hanson et al., 2017; Yu et al., 2018) is presented.
115
116
117　　**2. METHODS**
118
119　　　The aim of the present study is to find values for dH and dS of selected clusters (11 different
120　　clusters) such that modeled new particle formation (NPF) rates represent measured NPF rates
121　　from the CLOUD experiment with a small error. In order to perform this task, a model has been
122　　developed that calculates the NPF rates based on given concentrations of sulfuric acid and
123　　ammonia, relative humidity, RH, and temperature, T (Section 2.2). The data set from Kürten et
124　　al. (2016) for 125 neutral NPF rates is used to derive dH and dS. A best-fit thermodynamic data
125　　set is obtained by using an optimization method (Section 2.4). Moreover, the distributions of
126　　the probability density functions for each cluster are explored with a Monte Carlo method
127　　(Kupiainen-Määttä, 2016 and Section 2.5).

128

2.1 Experimental data from the CLOUD experiment

130

131   The experimental data used to develop the model were taken at the CLOUD (Cosmics
132 Leaving OUtdoor Droplets) chamber at CERN (European Organization for Nuclear Research).
133 The 26.1 m^3 stainless steel chamber allows conducting nucleation and growth experiments
134 under atmospherically relevant conditions regarding the trace gas concentrations, temperature,
135 relative humidity and ion concentrations (Kirkby et al., 2011). The chamber and the results for
136 different chemical systems have been described elsewhere in the literature (e.g., Kirkby et al.
137 2011; Almeida et al., 2013; Duplissy et al., 2016). In the present study no new data are presented
138 from CLOUD; instead the data from the Dunne et al. (2016) and Kürten et al. (2016) studies
139 are used. Whereas in the previous publications the influence of the ion concentration on
140 nucleation was also discussed, this study focuses on neutral nucleation only. The parameter
141 space covers temperatures between 208 K and 292 K (five different temperatures) and a wide
142 range of atmospherically relevant sulfuric acid and ammonia concentrations. No systematic
143 investigation of the relative humidity was carried out; for most experiments, the relative
144 humidity was at 38%. The new particle formation rates are reported for a mobility diameter of
145 1.7 nm (1.4 nm geometric diameter, see Ku and Fernandez de la Mora, 2009).

146

2.2 Acid base model

148

149   The model used in the present study solves a set of differential equations describing the
150 concentrations of clusters and particles (McMurry, 1980; Kürten et al., 2014; Kürten et al.,
151 2015a; McMurry and Li, 2017; Kürten et al., 2018). The model from Kürten et al. (2018)
152 describes nucleation for the system of sulfuric acid and dimethylamine, where the formed
153 clusters are stable against evaporation at a temperature of 278 K. For this reason, the system
154 can be treated as quasi-unary and the kinetic approach (all cluster evaporation rates equal zero)
155 yields very good agreement between modeled and measured particle concentrations and
156 formation rates over a wide range of particle diameters. The model treats the smallest clusters
157 in molecular size bins, based on the number of sulfuric acid molecules in a cluster, while
158 geometric size bins are used for the larger clusters/particles (Kürten et al., 2018). In the present
159 study 12 molecular bins and 25 geometric bins with a geometric growth factor of 1.25 result in
160 a maximum particle diameter of 295 nm. Compared with the earlier study by Kürten et al.
161 (2018) the number of bins is reduced in order to reduce computation time.
162   While the approach of using a quasi-unary system with zero evaporation worked well for
163 sulfuric acid-dimethylamine, this assumption cannot be used for sulfuric acid and ammonia
164 because some small clusters evaporate rapidly (Nadykto and Yu, 2007; Ortega et al., 2012; Jen
165 et al., 2014). In the following, the number of sulfuric acid molecules denotes the clusters as
166 monomers (1 sulfuric acid), dimers (2 sulfuric acids), trimers (3 sulfuric acids), etc. The clusters
167 from the monomer to the tetramer can contain different numbers of ammonia molecules, where
168 the maximum number of ammonia molecules is not allowed to exceed the number of acid
169 molecules. This results in the acid-base reaction scheme shown in Figure 1, where A_1 denotes
170 the sulfuric acid monomer concentration and B_1 the ammonia concentration. For the larger
171 clusters and particles (starting with the pentamer), no differentiation regarding the base content

Atmospheric
Chemistry
and Physics
Discussions

172   is applied. The full set of differential equations used in SANTIAGO (Sulfuric acid Ammonia
173   NucleaTIon And GrOwth model) is listed in SI Text1. Compared with its previous version
174   SANTIAGO can more accurately describe nucleation from sulfuric acid and ammonia because
175   of the consideration of clusters with different amounts of acid and base that are allowed to
176   evaporate.

177   While a mixed acid-base cluster can in principle loose either acid or base, the following rule
178   was implemented in the model: clusters containing more acid than base can only evaporate an
179   acid molecule, while clusters containing equal numbers of acid and base can loose a base
180   molecule only. While this is a simplification of the reality, quantum chemical calculations
181   support that this assumption generally considers the dominant evaporation processes (Yu et al.,
182   2018). In principle, acid and base evaporation could be implemented for each cluster in the
183   model but this would increase the number of free parameters from 22 (with the simplification)
184   to 40 (with all possible evaporations) which would probably not lead to better results but
185   increase the computation time significantly. The existence of clusters containing more base than
186   acid is excluded in SANTIAGO, which is also supported by quantum chemical calculations
187   (Ortega et al., 2012; Yu et al., 2018).

188   The thermodynamic parameters for the two smallest pure acid clusters (A_2 and A_3) are taken
189   from Hanson and Lovejoy (2006). In their study, Hanson and Lovejoy report dependencies of
190   the dimer and trimer evaporation rates regarding the relative humidity, which are also adopted
191   in the present study (evaporation rate proportional to $(20\%/RH)^{0.5}$ for the dimer and
192    $(20\%/RH)^{1.5}$ for the trimer). The same dependency was used here and the evaporation rate for
193   the pure tetramer (A_4) was scaled by the same RH-dependent factor as for the pure acid trimer.
194   Further humidity effects are not applied; therefore, the results for the thermodynamic data can
195   be interpreted as a weighted average over the range of the different water contents for each
196   cluster. The equations for calculating an evaporation rate from dH and dS are given in SI Text2
197   (see also Ortega et al., 2012). In general, slower evaporation rates result from more negative
198   values of dH and from less negative values of dS; the evaporation rate varies exponentially with
199   dH and dS. How strong the evaporation rate varies with temperature, is determined by the value
200   of dH.

201   Forward reaction rates are calculated based on the equations for the collision frequency
202   function by Chan and Mozurkewich (2001) with a value of 6.4×10^{-20} J for the Hamaker constant
203   (Hamaker, 1937). An enhanced collision-rate between small clusters and particles due to van
204   der Waals forces was reported in recent CLOUD publications (Kürten et al., 2014; Lehtipalo et
205   al., 2016; Kürten et al., 2018). SANTIAGO takes into account dilution and wall loss, which are
206   relevant loss processes in the CLOUD chamber (Kirkby et al., 2011; Kürten et al., 2015a; SI
207   Text1). The value of the modeled new particle formation rate, J_{model}, is taken for the nonamer
208   (Kürten et al., 2015b):

210
$$J_{model} = \sum_{i+j \geq m} K_{i,j} \cdot N_i \cdot N_j. \tag{1}$$

212   The nonamer ($m = 9$) has approximately a mobility diameter of 1.7 nm for which CLOUD new
213   particle formation rates are derived (Kirkby et al., 2011; Dunne et al., 2016). The formation rate
214   calculation takes into account that the collision of two smaller clusters with concentrations N_i
215   and N_j yield a particle equal or larger than the nonamer. The differential equations are integrated

216   over the same time that each of the 125 individual CLOUD runs lasted; this time varied between
217   roughly half an hour and several hours dependent on the gas concentrations. The latest value of
218   the calculated nucleation rate defines the modeled NPF rate. Further details regarding the model
219   can be found in Kürten et al. (2015a, 2018) and in SI Text1.
220   The particle growth rates, GR, can be calculated using the monomer and cluster concentrations
221   in SANTIAGO:
222
223    $$GR_m = \sum_{i=1}^{m-1} \frac{\pi/6 \cdot d_{p,i}^3}{\pi/2 \cdot d_{p,m}^2} \cdot K_{m,i} \cdot N_i. \tag{2}$$
224
225   The increase in diameter depends on the particle diameter for which the growth rate is
226   determined, $d_{p,m}$, and the colliding cluster/particle diameter, $d_{p,i}$ (Nieminen et al., 2010). Note
227   that equation (2) does not only consider the growth due to monomer additions ($i = 1$) but also
228   the gain due to collisions with all clusters/particles smaller than the considered diameter.
229   Lehtipalo et al. (2016) have highlighted the importance of such cluster-cluster or cluster-particle
230   collisions, especially for systems containing high cluster concentrations like the sulfuric acid-
231   dimethylamine system. In the present study GR is calculated for $m = 9$, which corresponds to a
232   mobility diameter of 1.7 nm.
233
234   **2.3 Metric for average error of the model**
235
236   In order to optimize the thermodynamic parameters it is necessary to define a criterion that
237   describes the overall deviation between the 125 measured and modeled new particle formation
238   rates. Since the NPF rates span a large range (from roughly 10^{-3} to 10^2 cm^{-3} s^{-1}) it is reasonable
239   to compare the ratios between modeled and measured rates rather than the absolute differences.
240   In this way, it is avoided that mainly the high values of the NPF rates are brought into
241   agreement. In addition, it is taken into account that the data covers five different temperatures
242   (208, 223, 248, 278 and 292 K) with different numbers of experiments conducted at each of the
243   temperatures. In order to weigh each of the temperatures equally and not to bias the error
244   calculation towards the temperature where most of the experiments were conducted at the
245   following error function, f, was defined:
246

247    $$f = log\left(\frac{1}{5} \cdot \left(\frac{1}{n_1} \cdot \sum_{i=1}^{n_1} 10^{|log(J_{model,i}) - log(J_{exp,i})|} + \frac{1}{n_2} \cdot \sum_{i=1}^{n_2} 10^{|log(J_{model,i}) - log(J_{exp,i})|} + \right. \right.$$

248    $$\frac{1}{n_3} \cdot \sum_{i=1}^{n_3} 10^{|log(J_{model,i}) - log(J_{exp,i})|} + \frac{1}{n_4} \cdot \sum_{i=1}^{n_4} 10^{|log(J_{model,i}) - log(J_{exp,i})|} + \frac{1}{n_5} \cdot$$

249    $$\left. \left. \sum_{i=1}^{n_5} 10^{|log(J_{model,i}) - log(J_{exp,i})|} \right) \right) \tag{3}$$

250
251   In this equation the values n_1 to n_5 indicate the number of experiments at each temperature.
252
253   **2.4 Optimization method**
254

Atmospheric
Chemistry
and Physics
Discussions

Open Access

255   The optimization method used was introduced by Steihaug (1983) and uses an
256   approximation for the function, f, that should be minimized. A quadratic model (second order
257   Taylor expansion) approximates the function:

258

259      $M(x_k + s_k) = f(x_k) + g_k^T \cdot s_k + \frac{1}{2} \cdot s_k^T H_k s_k.$ (4)

260

261   In this study, the point x_k is the current set of thermodynamic parameters (11 dH and 11 dS
262   values, i.e., 22 parameters in total) and s_k is the vector that moves the point to a new position
263   that ideally yields a smaller error (i.e., a smaller value for f). The gradient vector is denoted by
264   g_k and the Hessian matrix by H_k. Steihaug's conjugated gradient method finds s_k that minimizes
265   M (Steihaug, 1983; Nocedal and Wright, 2006). The algorithm takes into account that the length
266   of the vector s_k stays within a certain trust region, Δ_k (i.e., $\|s_k\| \leq \Delta_k$). The value of

267

268      $\rho_k = \frac{f(x_k) - f(x_k + s_k)}{M(x_k) - M(x_k + s_k)}$ (5)

269

270   is used to decide whether Δ_k can be increased, stays unchanged or should be reduced after each
271   iteration, k. The empirical factor η_1 is used to determine after each iteration whether a step
272   should be taken or not:

273

274      $x_{k+1} = \begin{cases} x_k + s_k & \rho_k \geq \eta_1 \\ x_k & \rho_k < \eta_1 \end{cases}.$ (6)

275

276   The trust region radius is updated by using the following rules:

277

278      $\Delta_{k+1} = \begin{cases} t_1 \cdot \Delta_k & \rho_k < \eta_2 \\ min(t_2 \cdot \Delta_k, \Delta_{max}) & \rho_k \geq \eta_3 \\ \Delta_k & \eta_2 \leq \rho_k < \eta_3 \end{cases},$ (7)

279

280   where the empirical parameters η_2, η_3, t_1 and t_2 are used. The algorithm in this study was run
281   with parameters $\Delta_0 = 0.5$, $\Delta_{max} = 2$, $t_1 = 0.25$, $t_2 = 2.0$, $\eta_1 = 0.20$, $\eta_2 = 0.25$, $\eta_3 = 0.75$ and
282   converged approximately after 20 steps. The values for x_0 (initialization) are the dH and dS
283   values from Ortega et al. (2012).

284

285   **2.5 Monte Carlo method**

286

287   With the Monte Carlo method (Differential Evolution-Markov Chain algorithm, DE-MC,
288   see Ter Braak, 2006; Ter Braak and Vrugt, 2008; Kupiainen-Määttä, 2016) the probability
289   density functions (pdf) of the thermodynamic parameters are explored. The pdf give
290   information on the uncertainties of the parameters found by the optimization algorithm, as it is
291   very likely that the optimized values represent a local minimum in the parameter space that is
292   just one possible solution out of many others. The DE-MC algorithm aims at finding the most
293   probable values for the parameters instead of finding the optimal values (Kupiainen-Määttä,
294   2016). Therefore, the Monte Carlo solutions can be used to evaluate if the optimized values
295   are within the range of the most probable solutions.

Atmospheric
Chemistry
and Physics
Discussions

296

2.5.1 Initialization for generating the prior distributions

297

298

299   At the start of the Monte Carlo simulation, the parameters dH and dS are initialized, where
300   each value is randomly selected from a range of possible values. In this study, this range was
301   defined by the values from Ortega et al. (2012) $\pm$ 10 kcal mol^{-1} for dH and $\pm$ 10 cal mol^{-1} K^{-1}
302   for dS. For these randomly selected thermodynamic parameters, the initial error (equation (3))
303   is calculated.

304

2.5.2 Main loop

305

306

307   Within the main loop (iterated 5000 times), the first step involves the random variation of
308   the parameters. The value for each dH and dS is updated with a probability of 0.2. Given that
309   22 parameters are used, this means that on average 4.4 parameters changed during each
310   iteration. If, however, the situation occurs that no update for any of the parameters is requested,
311   the selection process is repeated until at least one thermodynamic parameter is updated
312   (Kupiainen-Määttä, 2016). If a value should be updated its step width is chosen from a normal
313   distribution with a standard deviation of 0.05 times the width of the allowed range (i.e., 20 kcal
314   mol^{-1} for dH and 20 cal mol^{-1} K^{-1} for dS). If a step would lead to the crossing of the upper or
315   lower bound for any of the parameters, a new random value is chosen until the updated value
316   stays within its allowed range. With the new set of parameters, the new error, $f(x_k + s_k)$, is
317   calculated. If $f(x_k + s_k) < f(x_k)$, then the new set of parameters is accepted. However, even if $f(x_k + s_k)$
318     $+ s_k)$ is larger than $f(x_k)$ the step might still be accepted with the probability

319

320     $$P = exp\left(-\frac{1}{2\sigma^2} \cdot \left(f(x_k + s_k) - f(x_k)\right)\right), \qquad (8)$$

321   where a σ of 0.2 has been chosen (same as by Kupiainen-Määttä, 2016). This means that even
322   steps in the "wrong" direction (making the error larger) have a chance of being taken. This can
323   avoid that the parameters might become trapped in a local minimum, which can, e.g., be the
324   case with minimization methods. In any case, x_{k+1} is set to $x_k + s_k$ if a step is taken before a new
325   iteration starts. The error as well as the full set of parameters are recorded after each iteration.

326

2.5.3 Generation of the prior distribution

327

328

329   In total 20 data sets (each containing 5000 steps) are generated with the methods described
330   in Section 2.5.1 and 2.5.2. From each of the 20 data sets the average error was determined from
331   the last 2500 points. Whenever the error for one data set is smaller than the geometric mean
332   from all 20 errors, the data set was selected (Kupiainen-Määttä, 2016). All selected data sets
333   combined and thinned to 5000 data points represent the prior distribution, Z_0. For each
334   parameter the standard deviation σ_{ini} is determined.

335

2.5.4 DE-MC algorithm

336

337

Atmospheric
Chemistry
and Physics
Discussions

338   In the DE-MC (Differential Evolution-Markov Chain) algorithm, five Markov chains are run
339   in parallel, where each of the chain starts from a random point of the joint history, Z_0 (Ter Braak,
340   2006; Ter Braak and Vrugt, 2008; Kupiainen-Määttä, 2016). In the algorithm, the probability
341   to jump from an old point, x_{old}, to a new point, x_{new}, should be the same as moving from x_{new} to
342   x_{old}. This is achieved, by calculating the new position vector according to
343
344    $$x_{new} = x_{old} + \gamma \cdot (x_1 - x_2) + \delta, \tag{9}$$
345
346   where x_1 and x_2 are randomly selected points from the joint history, Z_0. The factor γ is taken as
347   (Ter Braak, 2006)
348
349    $$\gamma = \frac{2.38}{\sqrt{2 \cdot n_{coefs}}} = \frac{2.38}{\sqrt{2 \cdot 22}} = 0.359 \tag{10}$$
350
351   or 0.98 (at every fifth step). Each individual dH and dS value for the new point is updated with
352   a probability of 0.2 (see Section 2.3.2). δ is drawn from a normal distribution with $\sigma = 0.05 \times \sigma_{ini}$
353   (calculated from the prior distribution, see above). The decision process whether a step should
354   be accepted or not is the same as in Section 2.5.2 (equation (8)).
355   The points from the five chains are appended to the joint history, Z_0, and the new points in
356   the following iterations are drawn from the updated history. This way, eventually convergence
357   should be reached after many iterations resulting in the posterior distributions (probability
358   density functions) for all parameters. The metric indicating convergence is given by
359   (Kupiainen-Määttä, 2016):
360
361    $$\hat{R} = \frac{k-1}{k} + \frac{c+1}{c} \cdot \frac{b}{W}, \tag{11}$$
362
363   with the parameter k indicating the step index; the number of chains is $c = 5$. The variance of
364   the means for each parameter, b, is calculated from
365
366    $$b = \frac{1}{c} \cdot \sum_{l=1}^{c} (\bar{\mu} - \mu_l)^2, \tag{12}$$
367
368   where $\bar{\mu}$ is the average of a parameter over all chains and μ_l is the average for each of the chains,
369   l. The mean of the variances, W, is calculated from
370
371    $$W = \frac{1}{c} \cdot \sum_{l=1}^{c} Var_l, \tag{13}$$
372
373   where Var_l is the variance for each parameter in one of the chains. Convergence is assumed
374   when $\hat{R}$ (for each of the 22 parameters) reaches a value of < 1.1. In the present study, this was
375   the case after more than 10^5 iterations.
376
377
378   **3. RESULTS**
379

Atmospheric
Chemistry
and Physics
Discussions

3.1 Thermodynamic data

The results for the thermodynamic parameters are shown in Figure 2. This figure indicates the results from the optimization method (dashed lines) and the probability density functions (pdf, solid lines) along with their medians (dotted lines) for the 11 different clusters. A comparison between the pdf and the values from Ortega et al. (2012) and Hanson et al. (2017) is shown in Figure S1. The pdf result from generating histograms of the values from Z_0, where the first 5000 points are neglected (see Section 2.5.4). Discussion on the thermodynamic data follows in Section 4.

An overall comparison between modeled and measured NPF rates is shown in Figure 3. SANTIAGO uses the thermodynamic data from Steihaug's optimization method. The maximum ratio for the deviation between the modeled and measured nucleation rates is below a factor of 10 with only a few exceptions. The average deviation is a factor of ~4. Some of the cases where the ratio deviates by more than a factor of 10 correspond to the lowest temperature (208 K) binary experiments where the model overestimates the measured NPF rates (Section 3.2). As intended (Section 2.3) the data in Figure 3 do not indicate an apparent bias.

3.2 Comparison between modeled and experimental data: $J_{1.7nm}$ vs. [H_2SO_4]

To further evaluate the performance of SANTIAGO the calculated NPF rates are shown together with the measured rates as a function of the sulfuric acid concentration for the five different temperatures (Figure 4). The color code represents the ammonia mixing ratio, while grey symbols indicate pure binary nucleation (see Kürten et al., 2016; Duplissy et al., 2016). Again, as in Figure 3 the agreement between modeled and measured data is good. The same applies to the parameterization; in some cases, the parameterization yields even better agreement compared with the model. This is the case, e.g., for the binary nucleation at 208 K and the data at 278 K and 292 K for the lowest ammonia mixing ratios. However, one clear advantage of SANTIAGO is that it describes the functional behavior of the system more accurately. At a temperature of 208 K for the high ammonia mixing ratio the model line shows a pronounced curvature, whereas the parameterization yields a straight line on the log-log-plot. The curvature is due to the fact that the survival probability of subcritical clusters (i.e., clusters below the nonamer) can be strongly affected by wall loss (Ehrhart and Curtius, 2013). This effect is most strongly pronounced when the concentration of the nucleating vapor is relatively low, which results in slow cluster/particle growth rates. Other thermodynamic data sets can be used to generate model curves similar to the ones in Figure 4. Using the data from Ortega et al. (2012) and Hanson et al. (2017) generates Figure S3 and Figure S4. Figure S2 shows the model curves using dH and dS from the medians of the Monte Carlo simulation. The medians also give good results, except for an overestimation at 248 K and 278 K at the lowest NH_3 concentration. This is probably due to comparatively low dG values for the sulfuric acid tetramer (Table 1). Unfortunately, Yu et al. (2018) did not provide dH and dS values but only dG values at 298 K; therefore, their data set could not be tested.

3.3 Comparison between modeled and experimental data: $J_{1.7nm}$ vs. [NH_3]

424   SANTIAGO can yield the dependency of the NPF rates for varying ammonia concentrations
425   at fixed sulfuric acid concentration. Figure 5 shows these data for five different temperatures
426   over a wide range of NH_3 concentrations. The modeled data agree overall very good with the
427   experimental CLOUD data. The data points indicated in Figure 5 are obtained by normalizing
428   the CLOUD data to one sulfuric acid concentration for each of the temperatures (see Kürten et
429   al., 2016); the sulfuric acid concentrations for the normalization are indicated in the figure
430   annotation.
431   For the lowest temperature (208 K) the new particle formation rates show almost no increase
432   with [NH_3] when ammonia is present at low concentrations ($\leq 10^6$ cm^{-3}); this indicates that NPF
433   is dominated by the pure binary channel. The data points for pure binary conditions are placed
434   at the estimated NH_3 background concentrations for 208 K and 223 K in Figure 5 (Kürten et
435   al., 2016). However, in the model for generating the lines at pure binary conditions (Figure 4),
436   zero NH_3 is assumed. For larger [NH_3] the NPF rates increase until they reach a plateau at ($\geq$
437   10^9 cm^{-3}). In this case new particle formation is only limited by the availability of sulfuric acid;
438   evaporating ammonia molecules from clusters are, however, rapidly replaced because the
439   arrival rate of ammonia is similar or faster than the ammonia evaporation rate. For the data at
440   223 K the situation is very similar. The plateau values agree very well with the calculated values
441   for collision-controlled new particle formation (Kürten et al., 2018), which can be seen as a
442   validation of SANTIAGO.
443   For both temperatures (208 K and 223 K) the experimental pure binary new particle
444   formation rates are well represented by the model. At 248 K and above, the modeled rates at
445   low [NH_3] very likely overestimate the NPF rates (dashed sections of the curves, see discussion
446   in Section 4) because the model considers only evaporation up to the sulfuric acid tetramer,
447   which is not sufficient to accurately model binary nucleation at these conditions. For higher
448   [NH_3] the rates increase steeply. Although the slopes of the curves flatten somewhat towards
449   high ammonia concentrations, no plateau is reached even at concentrations of 10^{11} cm^{-3}
450   (approximately 4 ppbv).

3.4 Particle growth rates

454   Figure 6 shows calculated growth rates as a function of the sulfuric acid concentration
455   according to equation (2). Additionally, a curve from the equations given by Nieminen et al.
456   (2010) is included. The model results from the present study show a linear increase in *GR* as a
457   function of the sulfuric acid monomer concentration as expected (Nieminen et al., 2010). The
458   higher values from SANTIAGO can be explained by the different methods for calculating the
459   collision rate constant that includes van der Waals enhancement for the model of the present
460   study (c.f. Kürten et al., 2018). The increase in *GR* at low temperature (208 K) is not intuitive
461   as the collision rates decrease somewhat with temperature, which should lead to slower *GR*.
462   However, the clusters are more stable at low temperature and their elevated concentrations can
463   contribute to particle growth (Lehtipalo et al., 2016). This effect is pronounced at 208 K with
464   some ammonia. The possibility of deriving growth rates with the model is an important
465   advantage over a parameterization. It enables further comparison to experimental data and the
466   future study of particle growth to climatically relevant diameters.

Atmospheric
Chemistry
and Physics
Discussions

468

4. DISCUSSION

469

470

4.1 General discussion on the thermodynamic values

471

472

4.1.1 Results from the optimization and Monte Carlo method

473

474

475   The posterior distributions with the median values for dH and dS for all clusters are shown
476   in Figure 2. For comparison, the values from Steihaug's optimization method are also shown.
477   For the dS values, the medians and the optimized values agree very well. However, the
478   distributions are rather flat indicating that there is a wide possible range of entropies that lead
479   to reasonable agreement between modeled and measured NPF rates. This is also reflected in
480   Table 1 when comparing the dS to the Ortega et al. (2012) data. These were used to initialize
481   the optimization method. However, no large differences can be found between the initialized
482   and optimized values.

483   The distributions for the dH values show more structure. However, the only cluster where a
484   clear peak can be found is the A_2B_2 cluster (for the B evaporation). The median value of the
485   distribution is somewhat lower (by ~2 kcal mol^{-1}) compared with the optimized value but it is
486   well within the half-width of the distribution. For most dH values there exist flat regions of the
487   probability density function, e.g., for the A_2B_1 cluster (A evaporation) between -28 kcal mol^{-1}
488   and -39 kcal mol^{-1}. In this range the evaporation rate varies between 5×10^{-3} s^{-1} and 1×10^{-11} s^{-1}
489   (at 278 K and dS = -43 cal mol^{-1} K^{-1}, SI Text2). In practice, it does not matter which one of
490   these evaporation rates is used; the magnitude of the evaporation rate in this range has
491   essentially no effect on the outcome because the cluster is stable on the considered time-scale
492   (Kupiainen-Määttä, 2016).

493   For some clusters, limits seem to exist for dH. For example, the dH value for the A_4 is below
494   -15 kcal mol^{-1} and for the A_4B_3 clusters (A evaporation) the upper limit is approximately -19
495   kcal mol^{-1}. The pdf for the A_1B_1 and the A_2B_1 clusters show local maxima, which indicate
496   elevated probability densities around -16.5 kcal mol^{-1} and -23 kcal mol^{-1}.

497

4.1.2 Comparison of dH and dS to literature data

498

499

500   For most of the clusters, the agreement between the Ortega et al. (2012) data and the data
501   from the present study is quite good. One exception, is the A_4 cluster, where the pdf indicates
502   a median value of -23.1 kcal mol^{-1} for dH (-19.7 kcal mol^{-1} from the optimization method) in
503   contrast to -16.78 kcal mol^{-1} by the Ortega et al. (2012) study. The much lower value found in
504   the present study is reasonable since Ortega et al. (2012) did not include water vapor in their
505   calculations. The available water in the CLOUD experiment can lead to significant slower
506   evaporation rates indicated by the lower dH value. The difference to the Hanson et al. (2017)
507   data is generally much larger. Especially, the trimer and tetramer with one ammonia (A_3B_1 and
508   A_4B_1) evaporate significantly slower for the Hanson et al. (2017) data. This might explain the
509   much higher NPF rates observed at the warm temperatures for the Hanson et al. (2017)
510   predictions compared with the CLOUD data (Figure S4). Yu et al. (2018) report dG values
511   (Table 1) in their study. While the agreement between their model and CLOUD data is generally

512 good for ion-induced conditions, the agreement for neutral conditions is only good for low
513 temperature conditions. At temperatures $\geq$ 248 K the Yu et al. (2018) model underestimates the
514 measurements by up to many orders of magnitude. This can at least partly be explained by the
515 significantly higher dG values for some clusters (e.g., A_2B_1 and A_4B_1) in comparison to the
516 other literature data and the values from the present study.

517

518 **4.2 Uncertainties and limitations of SANTIAGO**

519

520 One limitation of the model from the present study is that the effect of water vapor is not
521 taken into account explicitly, i.e., no clusters containing different amounts of water molecules
522 are considered. However, for the clusters containing no ammonia to some extent humidity
523 effects are included. This is achieved by scaling the evaporation rates of the sulfuric acid dimer,
524 trimer and tetramer by a factor $(20\% / RH)^p$ with $p = 0.5$ for the dimer and 1.5 for the trimer
525 and tetramer. The first two values for the parameter p are from Hanson and Lovejoy (2006).
526 For the tetramer the same dependency as for the trimer is assumed, which introduces
527 uncertainty. The reported dH and dS values for the sulfuric acid tetramer are therefore derived
528 for a relative humidity of 20% in order to be consistent with the Hanson and Lovejoy (2006)
529 data. In Figure 4 the agreement between the modeled and measured pure binary data (at 208 K
530 and 223 K) is relatively good, especially for the 223 K data. For the 208 K data SANTIAGO
531 overestimates the measured data. It has to be noted, that the model calculations assume an
532 average RH (33% at 208 K and 28% at 223 K), whereas the measurement conditions cover
533 varying relative humidities (12% to 57% at 208 K and 11% to 52% at 223 K). This can explain
534 some of the scatter in the measured data but not the systematic overestimation for the 208 K
535 data by the model. However, the general agreement between model and measurement at $\leq$ 223
536 K is considered good for both ternary and binary conditions. For the warmer temperatures ($\geq$
537 248 K) the pure binary conditions can currently not be accurately represented by the model.
538 This can be seen in Figure 5 for the dashed sections of the curves, which approximately mark
539 the limit of the parameter space regarding the allowed NH_3 concentrations. For the very low
540 NH_3 concentrations, the modeled NPF rates approach the "pure" binary conditions. However,
541 comparison with the data by Ehrhart et al. (2016) who simulated pure binary nucleation for the
542 CLOUD chamber with the SAWNUC (Sulfuric Acid Water NUCleation) model indicate that
543 the apparent binary data in Figure 5 is significantly overestimating the true binary NPF rates.
544 For 248 K the overestimation seems to be within a factor of 10 but for 278 K and 292 K the
545 overestimation amounts to many orders of magnitude (Ehrhart et al., 2016). For this reason, the
546 solid line sections for 248 K and warmer have been defined such that the contribution from the
547 overestimated binary conditions is in any case less than 10%. This means that SANTIAGO can
548 be applied, e.g., at 292 K for NH_3 concentrations above ca. 1×10^7 cm^{-3} ($\approx$ 0.4 pptv). It can be
549 seen that NH_3 has a large effect even at these tiny concentrations, which are below the
550 measurable range of ammonia in the atmosphere.
551 The effect of water vapor on particle growth rates needs to be studied in the future.
552 Comparison between measured and modeled growth rates at small diameters (2 nm) in the acid
553 base system (sulfuric acid-dimethylamine and sulfuric acid-ammonia) indicates that water has
554 no significant effect on particle growth (Lehtipalo et al., 2016). The same can be concluded for
555 the sulfuric acid-ammonia system at larger diameters (~10 nm, see Chen et al., 2018).

Atmospheric
Chemistry
and Physics
Discussions

556   The fact that no larger clusters than the tetramers can evaporate in SANTIAGO apparently
557 leads to truncation errors as discussed before for the binary conditions. This truncation leads to
558 the overestimation of new particle formation rates for the pure binary conditions at the warm
559 temperatures. To what extent truncation affects the ternary new particle formation can be
560 discussed based on the cluster evaporation rates for the tetramers at the warmest temperature
561 (292 K). The evaporation rates are ~3000 s^{-1} (A_4B_1), ~75 s^{-1} (A_4B_2) and ~0.02 s^{-1} (A_4B_3) using
562 the thermodynamic parameters from Table 1 (first columns) and the equations to convert dH
563 and dS to an evaporation rate (see SI Text2). This indicates that new particle formation proceeds
564 most efficiently via the clusters containing at least three base molecules. For this cluster the
565 forward reaction rate is larger than the evaporation rate when the total sulfuric acid
566 concentration is larger than ~2×10^7 cm^{-3}. If the A_4B_3 and A_4B_4 clusters are the dominant ones,
567 this indicates that even if a pentamer with a small number of base molecules evaporates rapidly
568 it is probably not very important in terms of contributing to the new particle formation rates as
569 the main nucleation pathway will follow the clusters with high ammonia content. If truncation
570 nevertheless plays a role, it can lead to an overestimation of evaporation for a smaller cluster,
571 thereby compensating for the missing evaporation of the larger clusters. Therefore, it is possible
572 that some evaporation rates in the present study could be overestimated. However, the data that
573 are shown in Table 1 for a comparison have been derived from similar methods, where the
574 effect of evaporation is also considered only up to a certain cluster size limit. Truncation effects
575 are discussed in detail by Hanson et al. (2017).
576   Similarly, to truncation the negligence of evaporation of either acid or base for all considered
577 clusters can potentially lead to errors (see Section 2.2). The model includes only the cluster
578 evaporation rates, which seem to be most relevant (see Figure 1 and cf. Ortega et al., 2012; Yu
579 et al., 2018). For each cluster, one evaporation rate is included (either acid or base). This means,
580 that the negligence of the second evaporation channel can lead to an overestimation of the
581 cluster concentration. However, in case the omitted evaporation rate is smaller than the
582 considered one, this effect is very likely small. The selection of the considered evaporation rates
583 are guided by the literature data on QC calculations (Ortega et al., 2012; Yu et al., 2018). This
584 does, however, not rule out that important evaporation channels could be neglected. On the
585 other hand, increasing the number of free parameters does not necessarily improve the accuracy
586 of the model but only its complexity and the computational demands for the optimization and
587 Monte Carlo calculations.

589 **4.3 Implementation of literature data in SANTIAGO**

591   The previous study by Kürten et al. (2016) compares the CLOUD data with ACDC
592 (Atmospheric Cluster Dynamics Code, McGrath et al., 2012) model calculations using the
593 thermodynamic data from Ortega et al. (2012). Using the same data Figure S3 shows this
594 comparison using the model from the present study. Surprisingly the agreement between model
595 and measurement is better than in the study by Kürten et al. (2016). One difference between the
596 two studies is that the ACDC model used the formation rate for neutral clusters containing six
597 sulfuric acid molecules instead of nine in the present study. This difference was tested with the
598 present model but it does only lead to a very small change in the simulated formation rates. An
599 effect that can, however, explain the discrepancy is that the ACDC model calculations did not

Atmospheric
Chemistry
and Physics
Discussions

600   consider a wide range of particle sizes. This could lead to inaccuracies regarding the coagulation
601   sink for the formed clusters. Especially at high acid concentrations when growth and nucleation
602   rates are large, the particles can create a significant sink that can reach similar magnitude as the
603   wall loss rate in the CLOUD chamber (Kürten et al., 2015b). Neglecting the full size distribution
604   can lead to an overestimation of cluster concentrations and formation rates (SI Text1). This
605   effect needs to be studied in more detail in the future. In any case, taking into account particles
606   over a wide size range should improve the accuracy of a model due to the described effect.
607   The comparison between the CLOUD data and SANTIAGO using the Hanson et al. (2017)
608   data is shown in Figure S4. Hanson et al. base their data on flow tube measurements performed
609   at rather warm temperatures (~295 K). The agreement between the modeled and measured data
610   is good, however, mostly at the low temperatures (208 K and 223 K); for the warmer
611   temperatures, the model using the literature data significantly overestimates the NPF rates. This
612   can partly be due to the fact that the model does not include all possible evaporation effects
613   (acid and base for each cluster). Hanson et al. (2017) derived their data, however, by including
614   many more possible evaporation channels. Their negligence shifts the new particle formation
615   rates to higher values. It is likely that this effect is stronger at warm temperatures because at
616   very cold conditions the evaporation rates for the clusters are generally very low except for the
617   A_1B_1 cluster. For this cluster only one possible evaporation channel exists that is included in
618   the model. By including the new particle formation rates reported by Hanson et al. (2017) for
619   278 K at CLOUD chamber conditions (additional symbols in Figure S4 at 278 K), the
620   agreement is somewhat better but still significantly higher than the CLOUD data. Therefore,
621   the missing evaporation channels in this study cannot explain the full extent of the discrepancy.
622
623
624   **5. SUMMARY AND CONCLUSIONS**
625
626   The model (SANTIAGO, Sulfuric acid Ammonia NucleaTIon And GrOwth model)
627   describes new particle formation and growth from the reactions between sulfuric acid and
628   ammonia. The effect of water vapor is taken into account but the capability of simulating binary
629   nucleation is limited to low temperatures ($\leq$ 223 K) because cluster evaporation rates are only
630   considered up to the tetramer; at warmer temperatures evaporation of larger pure acid clusters
631   becomes important.
632   SANTIAGO implements evaporation of the smallest clusters, containing one to four sulfuric
633   acid molecules and a variable number of ammonia molecules. The thermodynamic data (dH
634   and dS) for 11 different channels is used to calculate evaporation rates as a function of
635   temperature. Two numeric methods have been applied to find the best set of parameters
636   (Steihaug algorithm) and their probability density functions (Differential Evolution-Markov
637   Chain algorithm, DE-MC). This is achieved by comparing the model output to the CLOUD
638   data set for neutral nucleation in the ternary system of sulfuric acid-water-ammonia (Dunne et
639   al., 2016; Kürten et al., 2016). The average ratio between modeled and measured data is found
640   to be as small as ~4 for a wide range of conditions (208 K to 292 K, sulfuric acid at
641   atmospherically relevant concentrations, e.g., $\geq 5\times10^5$ cm^{-3} at 208 K and $\leq 2\times10^9$ at 292 K)
642   when using the best fit parameters. SANTIAGO can very well represent the neutral measured

Atmospheric
Chemistry
and Physics
Discussions

643   CLOUD data for all tested conditions. This means that even binary neutral nucleation at the
644   lowest temperatures (208 K and 223 K) can be well described.

645   The optimization and the Monte Carlo method were successfully applied to explore the
646   landscape of the cluster thermodynamics for the nucleating system of sulfuric acid and
647   ammonia. However, the probability density functions from the DE-MC algorithm do not yield
648   a very clear picture of the most likely values for dH and dS as the derived probability density
649   functions are rather flat and indicate a wide range of probable values. Therefore, the parameters
650   reported in the present study have a rather high uncertainty. Future experiments and quantum
651   chemical calculations are necessary to narrow down these uncertainties.

652   Implementation of the literature data in the model indicates that the Ortega et al. (2012)
653   thermodynamic data describes the CLOUD data better than previously thought (Kürten et al.,
654   2016). This could be because of the negligence of large particles in the previous study. It seems
655   essential to include the larger nucleated particles in the model as these contribute to the sink for
656   the small nucleating clusters and particles. The Hanson et al. (2017) data overestimate the new
657   particle formation rates for the warm temperatures (278 K and 292 K). No direct comparison to
658   the Yu et al. (2018) is possible as no temperature-dependent evaporation rates can be calculated
659   from their reported dG values at 298 K.

660   SANTIAGO allows calculating new particle formation rates for a wide range of
661   experimental conditions (T, RH, sulfuric acid and ammonia concentration). In contrast to the
662   parameterization from Dunne et al. (2016) for the CLOUD data it is also capable of considering
663   different external sinks (e.g., due to chamber/flow tube walls in laboratory experiments or the
664   presence of pre-existing particles in the atmosphere) that can affect nucleation and particle
665   growth (Kerminen and Kulmala, 2002; Ehrhart and Curtius, 2013). With the model, growth
666   rates can also be determined.

667   Finally, the strong dependence on [NH$_3$] regarding NPF even at levels below 1 pptv
668   highlights the need for improved instrumentation when one wants to understand the impact of
669   ammonia on nucleation as no available technique can measure such low atmospheric ammonia
670   concentrations in real-time.

671
672

673   **DATA AVAILABILITY**

674

675   Data used in this study is available upon request by sending an email to the corresponding
676   author.

677
678

679   **AUTHOR CONTRIBUTION**

680

681   AK developed the numerical nucleation and growth model, implemented the optimization algorithms,
682   performed the modeling calculations and wrote the manuscript.

Atmospheric
Chemistry
and Physics
Discussions

Open Access

EGU

683 **Nomenclature**

684

685	b	variance of the means for each parameter (dH or dS)
686	B	Hessian matrix of f regarding all dH and dS values
687	c	number of chains
688	d_p	particle diameter
689	dH	enthalpy for one of the reactions (see Table 1)
690	dS	entropy for one of the reactions (see Table 1)
691	f	average error for all modeled and measured particle formation rates
692	g	gradient vector of f regarding all dH and dS values
693	GR	particle growth rate
694	i	index
695	j	index
696	J_{exp}	experimental formation rate (from CLOUD experiment)
697	J_{model}	modeled formation rate
698	k	iteration index in numeric algorithms
699	K	collision rate constant for clusters/particles
700	l	index
701	m	index for critical cluster size ($m = 9$)
702	M	approximated function value in Steihaug's method
703	n	number of experiments (n_1 for 208 K, n_2 for 223 K, n_3 for 248 K, n_4 for 278 K, n_5 for
704		298 K)
705	n_{coefs}	total number of coefficients, i.e., all dH and dS values ($n_{coefs} = 22$)
706	N	cluster/particle number density
707	p	power dependency of an evaporation rate regarding the relative humidity
708	P	acceptance probability in Monte Carlo algorithm
709	$\hat{R}$	statistical metric to indicate convergence for the Monte Carlo simulation
710	RH	relative humidity
711	s	vector of step changes (all dH and dS values) in one iteration
712	t	empirical parameter needed in Steihaug's optimization algorithm (t_1, t_2)
713	T	temperature
714	Var	variance for a parameter in one of the chains
715	W	mean of the variances over all chains for one parameter
716	x	current vector of all dH and dS values (Monte Carlo simulation)
717	x_1, x_2	drawn vectors of all dH and dS values from history (Monte Carlo simulation)
718	x_{new}	new vector of all dH and dS values (Monte Carlo simulation)
719	x_{old}	old vector of all dH and dS values (Monte Carlo simulation)
720	Z_0	joint history for all chains in the Monte Carlo simulation
721	δ	term in the calculation of the new vector in the Monte Carlo algorithm
722	Δ	radius of trust region in Steihaug's method
723	Δ_{max}	maximum allowed radius of trust region in Steihaug's method
724	γ	scaling factor in the calculation of the new vector in the Monte Carlo algorithm
725	η	empirical parameter needed in Steihaug's optimization algorithm (η_1, η_2, η_3)
726	μ	mean value for one parameter

727	$\bar{\mu}$	mean value over all chains for one parameter
728	ρ	ratio between actual and predicted function reduction in Steihaug's method
729	σ	standard deviation
730	σ_{ini}	standard deviation of the parameters from the prior distribution

Atmospheric
Chemistry
and Physics
Discussions

References

Almeida, J., Schobesberger, S., Kürten, A., Ortega, I. K., Kupiainen-Määttä, O., Praplan, A. P., Adamov, A., Amorim, A., Bianchi, F., Breitenlechner, M., David, A., Dommen, J., Donahue, N. M., Downard, A., Dunne, E. M., Duplissy, J., Ehrhart, S., Flagan, R. C., Franchin, A., Guida, R., Hakala, J., Hansel, A., Heinritzi, M., Henschel, H., Jokinen, T., Junninen, H., Kajos, M., Kangasluoma, J., Keskinen, H., Kupc, A., Kurtén, T., Kvashin, A. N., Laaksonen, A., Lehtipalo, K., Leiminger, M., Leppä, J., Loukonen, V., Makhmutov, V., Mathot, S., McGrath, M. J., Nieminen, T., Olenius, T., Onnela, A., Petäjä, T., Riccobono, F., Riipinen, I., Rissanen, M., Rondo, L., Ruuskanen, T., Santos, F. D., Sarnela, N., Schallhart, S., Schnitzhofer, R., Seinfeld, J. H., Simon, M., Sipilä, M., Stozhkov, Y., Stratmann, F., Tomé, A., Tröstl, J., Tsagkogeorgas, G., Vaattovaara, P., Viisanen, Y., Virtanen, A., Vrtala, A., Wagner, P. E., Weingartner, E., Wex, H., Williamson, C., Wimmer, D., Ye, P., Yli-Juuti, T., Carslaw, K. S., Kulmala, M., Curtius, J., Baltensperger, U., Worsnop, D. R., Vehkamäki, H., and Kirkby, J.: Molecular understanding of sulphuric acid-amine particle nucleation in the atmosphere, *Nature*, 502, 359–363, doi: 10.1038/nature12663, 2013.

Ball, S. M., Hanson, D. R., Eisele, F. L., and McMurry, P. H.: Laboratory studies of particle nucleation: Initial results for H_2SO_4, H_2O, and NH_3 vapors, *J. Geophys. Res.-Atmos.*, 104, D19, 23709–23718, doi: 10.1029/1999JD900411, 1999.

Benson, D. R., Erupe, M. E., and Lee, S.-H.: Laboratory-measured H_2SO_4-H_2O-NH_3 ternary homogeneous nucleation rates: Initial observations, *Geophys. Res. Lett.*, 36, L15818, doi: 10.1029/2009GL038728, 2009.

Chan, T. W., and Mozurkewich, M.: Measurement of the coagulation rate constant for sulfuric acid particles as a function of particle size using tandem differential mobility analysis, *J. Aerosol Sci.*, 32, 321–339, doi: 10.1016/S0021-8502(00)00081-1, 2001.

Chen, H., Chee, S., Lawler, M. J., Barsanti, K. C., Wong, B. M., and Smith, J. N.: Size resolved chemical composition of nanoparticles from reactions of sulfuric acid with ammonia and dimethylamine, *Aerosol Sci. Technol.*, 52, 1120–1133, doi: 10.1080/02786826.2018.1490005, 2018.

Chen, M., Titcombe, M., Jiang, J., Jen, C., Kuang, C., Fischer, M. L., Eisele, F. L., Siepmann, J. I., Hanson, D. R., Zhao, J., and McMurry, P. H.: Acid–base chemical reaction model for nucleation rates in the polluted atmospheric boundary layer, *P. Natl. Acad. Sci. USA*, 109, 18713–18718, doi: 10.1073/pnas.1210285109, 2012.

Atmospheric
Chemistry
and Physics
Discussions

770 Clarisse, L., Clerbaux, C., Dentener, F., Hurtmans, D., and Coheur, P.-F.: Global ammonia
771 distribution derived from infrared satellite observations, *Nature Geoscience*, 2, 479–483, doi:
772 10.1038/NGEO551, 2009.

774 Dunne, E. M., Gordon, H., Kürten, A., Almeida, J., Duplissy, J., Williamson, C., Ortega, I. K.,
775 Pringle, K. J., Adamov, A., Baltensperger, U., Barmet, P., Benduhn, F., Bianchi, F.,
776 Breitenlechner, M., Clarke, A., Curtius, J., Dommen, J., Donahue, N. M., Ehrhart, S., Flagan,
777 R. C., Franchin, A., Guida, R., Hakala, J., Hansel, A., Heinritzi, M., Jokinen, T., Kangasluoma,
778 J., Kirkby, J., Kulmala, M., Kupc, A., Lawler, M. J., Lehtipalo, K., Makhmutov, V., Mann, G.,
779 Mathot, S., Merikanto, J., Miettinen, P., Nenes, A., Onnela, A., Rap, A., Reddington, C. L. S.,
780 Riccobono, F., Richards, N. A. D., Rissanen, M. P., Rondo, L., Sarnela, N., Schobesberger, S.,
781 Sengupta, K., Simon, M., Sipilä, M., Smith, J. N., Stozkhov, Y., Tomé, A., Tröstl, J., Wagner,
782 P. E., Wimmer, D., Winkler, P. M., Worsnop, D. R., and Carslaw, K. S.: Global atmospheric
783 particle formation from CERN CLOUD measurements, *Science*, 354, 1119–1124, doi:
784 10.1126/science.aaf2649, 2016.

786 Duplissy, J., Merikanto, J., Franchin, A., Tsagkogeorgas, G., Kangasluoma, J., Wimmer, D.,
787 Vuollekoski, H., Schobesberger, S., Lehtipalo, K., Flagan, R. C., Brus, D., Donahue, N. M.,
788 Vehkämäki, H., Almeida, J., Amorim, A., Barmet, P., Bianchi, F., Breitenlechner, M., Dunne,
789 E. M., Guida, R., Henschel, H., Junninen, H., Kirkby, J., Kürten, A., Kupc, A., Määttänen, A.,
790 Makhmutov, V., Mathot, S. , Nieminen, T., Onnela, A., Praplan, A. P., Riccobono, F., Rondo,
791 L., Steiner, G., Tome, A., Walther, H., Baltensperger, U., Carslaw, K. S., Dommen, J., Hansel,
792 A., Petäjä, T., Sipilä, M., Stratmann, F., Vrtala, A., Wagner, P. E., Worsnop, D. R., Curtius, J.,
793 and Kulmala, M.: Effect of ions on sulfuric acid-water binary particle formation II:
794 Experimental data and comparison with QC-normalized classical nucleation theory, *J.
795 Geophys. Res.-Atmos.*, 121, 1752–1775, doi: 10.1002/2015JD023539, 2016.

797 Ehrhart, S. and Curtius, J.: Influence of aerosol lifetime on the interpretation of nucleation
798 experiments with respect to the first nucleation theorem, *Atmos. Chem. Phys.*, 13, 11465–
799 11471, doi: 10.5194/acp-13-11465-2013, 2013.

801 Ehrhart, S., Ickes, L., Almeida, J., Amorim, A., Barmet, P., Bianchi, F., Dommen, J., Dunne,
802 E. M., Duplissy, J., Franchin, A., Kangasluoma, J., Kirkby, J., Kürten, A., Kupc, A., Lehtipalo,
803 K., Nieminen, T., Riccobono, F., Rondo, L., Schobesberger, S., Steiner, G., Tomé, A., Wimmer,
804 D., Baltensperger, U., Wagner, P. E., and Curtius, J.: Comparison of the SAWNUC model with
805 CLOUD measurements of sulphuric acid-water nucleation, *J. Geophys. Res.-Atmos.*, 121,
806 12401–12414, doi: 10.1002/2015JD023723, 2016.

808 Elm, J., Bilde, M., and Mikkelsen, K. V.: Assessment of binding energies of atmospherically
809 relevant clusters, *Phys. Chem. Chem. Phys.*, 15, 16442, doi: 10.1039/c3cp52616j, 2013.

811 Elm, J., and Kristensen, K.: Basis set convergence of the binding energies of strongly hydrogen-
812 bonded atmospheric clusters, *Phys. Chem. Chem. Phys.*, 19, 1122, DOI: 10.1039/c6cp06851k,
813 2017.

814

815   Glasoe, W. A., Volz, K., Panta, B., Freshour, N., Bachman, R., Hanson, D. R., McMurry, P.
816   H., and Jen, C.: Sulfuric acid nucleation: An experimental study of the effect of seven bases, *J.*
817   *Geophys. Res. Atmos.*, 120, 1933–1950, doi: 10.1002/2014JD022730, 2015.

818

819   Gordon, H., Kirkby, J., Baltensperger, U., Bianchi, F., Breitenlechner, M., Curtius, J., Dias, A.,
820   Dommen, J., Donahue, N. M., Dunne, E. M., Duplissy, J., Ehrhart, S., Flagan, R. C., Frege, C.,
821   Fuchs, C., Hansel, A., Hoyle, C. R., Kulmala, M., Kürten, A., Lehtipalo, K., Makhmutov, V.,
822   Molteni, U., Rissanen, M. P., Stozhkov, Y., Tröstl, J., Tsagkogeorgas, G., Wagner, R.,
823   Williamson, C., Wimmer, D., Winkler, P. M., Yan, C., and Carslaw, K. S.: Causes and
824   importance of new particle formation in the present-day and preindustrial atmospheres, *J.*
825   *Geophys. Res. Atmos.*, 122, 8739–8760, doi: 10.1002/2017JD026844, 2017.

826

827   Hamaker, H. C.: The London–van der Waals attraction between spherical particles, *Physica*, 4,
828   1058–1072, doi: 10.1016/S0031-8914(37)80203-7, 1937.

829

830   Hanson, D. R., and Eisele, F. L.: Measurement of prenucleation molecular clusters in the NH_3,
831   H_2SO_4, H_2O system, *J. Geophys. Res. Atmos.*, 107, 4158, doi: 10.1029/2001JD001100, 2002.

832

833   Hanson, D. R., and Lovejoy, E. R.: Measurement of the thermodynamics of the hydrated dimer
834   and trimer of sulfuric acid, *J. Phys. Chem. A*, 110, 9525–9528, doi: 10.1021/jp062844w, 2006.

835

836   Hanson, D. R., Bier, I, Panta, B., Jen, C. N., and McMurry, P. H.: Computational Fluid
837   Dynamics Studies of a Flow Reactor: Free Energies of Clusters of Sulfuric Acid with NH_3 or
838   Dimethyl Amine, *J. Phys. Chem. A*, 121, 3976–3990, doi: 10.1021/acs.jpca.7b00252, 2017.

839

840   Höpfner, M., Volkamer, R., Grabowski, U., Grutter, M., Orphal, J., Stiller, G., von Clarmann,
841   T., and Wetzel, G.: First detection of ammonia (NH_3) in the Asian summer monsoon upper
842   troposphere, *Atmos. Chem. Phys.*, 16, 14357–14369, doi: 10.5194/acp-16-14357-2016, 2016.

843

844   Jen, C., McMurry, P. H., and Hanson, D. R.: Stabilization of sulfuric acid dimers by ammonia,
845   methylamine, dimethylamine, and trimethylamine, *J. Geophys. Res.-Atmos.*, 119, 7502–7514,
846   doi: 10.1002/2014JD021592, 2014.

847

848   Jen, C. N., Zhao, J., McMurry, P. H., and Hanson, D. R.: Chemical ionization of clusters formed
849   from sulfuric acid and dimethylamine or diamines, *Atmos. Chem. Phys.*, 16, 12513–12529, doi:
850   10.5194/acp-16-12513-2016, 2016.

851

852   Jokinen, T., Sipilä, M., Kontkanen, J., Vakkari, V., Tisler, P., Duplissy, E.-M., Junninen, H.,
853   Kangasluoma, J., Manninen, H. E., Petäjä, T., Kulmala, M., Worsnop, D. R., Kirkby, J.,
854   Virkkula, A., and Kerminen, V.-M.: Ion-induced sulfuric acid–ammonia nucleation drives
855   particle formation in coastal Antarctica, *Sci. Adv.*, 4, doi: 10.1126/sciadv.aat9744, 2018.

856

Atmospheric
Chemistry
and Physics
Discussions

857   Kerminen, V.-M., and Kulmala, M.: Analytical formulae connecting the "real" and the
858   "apparent" nucleation rate and the nuclei number concentration for atmospheric nucleation
859   events, *J. Aerosol Sci.*, 33, 609–622, doi: 10.1016/S0021-8502(01)00194-X, 2002.
860
861   Kirkby, J., Curtius, J., Almeida, J., Dunne, E., Duplissy, J., Ehrhart, S., Franchin, A., Gagné,
862   S., Ickes, L., Kürten, A., Kupc, A., Metzger, A., Riccobono, F., Rondo, L., Schobesberger, S.,
863   Tsagkogeorgas, G., Wimmer, D., Amorim, A., Bianchi, F., Breitenlechner, M., David, A.,
864   Dommen, J., Downard, A., Ehn, M., Flagan, R.C., Haider, S., Hansel, A., Hauser, D., Jud, W.,
865   Junninen, H., Kreissl, F., Kvashin, A., Laaksonen, A., Lehtipalo, K., Lima, J., Lovejoy, E. R.,
866   Makhmutov, V., Mathot, S., Mikkilä, J., Minginette, P., Mogo, S., Nieminen, T., Onnela, A.,
867   Pereira, P., Petäjä, T., Schnitzhofer, R., Seinfeld, J. H., Sipilä, M., Stozhkov, Y., Stratmann, F.,
868   Tomé, A., Vanhanen, J., Viisanen, Y., Vrtala, A., Wagner, P. E., Walther, H., Weingartner, E.,
869   Wex, H., Winkler, P. M., Carslaw, K. S., Worsnop, D. R., Baltensperger, U., and Kulmala, M.:
870   Role of sulphuric acid, ammonia and galactic cosmic rays in atmospheric aerosol nucleation,
871   *Nature*, 476, 429–435, doi: 10.1038/nature10343, 2011.
872
873   Ku, B. K., and Fernandez de la Mora, J.: Relation between electrical mobility, mass, and size
874   for nanodrops 1–6.5 nm in diameter in air, *Aerosol Sci. Technol.*, 43, 241–249, doi:
875   10.1080/02786820802590510, 2009.
876
877   Kupiainen-Määttä, O.: A Monte Carlo approach for determining cluster evaporation rates from
878   concentration measurements, *Atmos. Chem. Phys.*, 16, 14585–14598, doi: 10.5194/acp-16-
879   14585-2016, 2016.
880
881   Kürten, A., Jokinen, T., Simon, M., Sipilä, M., Sarnela, N., Junninen, H., Adamov, A., Almeida,
882   J., Amorim, A., Bianchi, F., Breitenlechner, M., Dommen, J., Donahue, N. M., Duplissy, J.,
883   Ehrhart, S., Flagan, R. C., Franchin, A., Hakala, J., Hansel, A., Heinritzi, M., Hutterli, M.,
884   Kangasluoma, J., Kirkby, J., Laaksonen, A., Lehtipalo, K., Leiminger, M., Makhmutov, V.,
885   Mathot, S., Onnela, A., Petäjä, T., Praplan, A. P., Riccobono, F., Rissanen, M. P., Rondo, L.,
886   Schobesberger, S., Seinfeld, J. H., Steiner, G., Tomé, A., Tröstl, J., Winkler, P. M., Williamson,
887   C., Wimmer, D., Ye, P., Baltensperger, U., Carslaw, K. S., Kulmala, M., Worsnop, D. R., and
888   Curtius, J.: Neutral molecular cluster formation of sulfuric acid-dimethylamine observed in
889   real-time under atmospheric conditions, *P. Natl. Acad. Sci. USA*, 111, 15019–15024, doi:
890   10.1073/pnas.1404853111, 2014.
891
892   Kürten, A., Münch, S., Rondo, L., Bianchi, F., Duplissy, J., Jokinen, T., Junninen, H., Sarnela,
893   N. Schobesberger, S., Simon, M., Sipilä, M. Almeida, J., Amorim, A., Dommen, J., Donahue,
894   N. M., Dunne, M., Flagan, R. C., Franchin, A., Kirkby, J., Kupc, A., Makhmutov, V., Petäjä,
895   T. Praplan, A. P., Riccobono, F., Steiner, G., Tomé, A., Tsagkogeorgas, G., Wagner, P. E.,
896   Wimmer, D., Baltensperger, U., Kulmala, M., Worsnop, D. R., and Curtius, J.:
897   Thermodynamics of the formation of sulfuric acid dimers in the binary (H_2SO_4-H_2O) and
898   ternary (H_2SO_4-H_2O-NH_3) system, *Atmos. Chem. Phys.*, 15, 10701–10721, doi: 10.5194/acp-
899   15-10701-2015, 2015a.
900

901   Kürten, A., Williamson, C., Almeida, J., Kirkby, J., and Curtius, J.: On the derivation of particle
902   nucleation rates from experimental formation rates, *Atmos. Chem. Phys.*, 15, 4063–4075, doi:
903   10.5194/acp-15-4063-2015, 2015b.

905   Kürten, A., Bianchi, F., Almeida, J., Kupiainen-Määttä, O., Dunne, E. M., Duplissy, J.,
906   Williamson, C., Barmet, P., Breitenlechner, M., Dommen, J., Donahue, N. M., Flagan, R. C.,
907   Franchin, A., Gordon, H., Hakala, J., Hansel, A., Heinritzi, M., Ickes, L., Jokinen, T.,
908   Kangasluoma, J., Kim, J., Kirkby, J., Kupc, A., Lehtipalo, K., Leiminger, M., Makhmutov, V.,
909   Onnela, A., Ortega, I. K., Petäjä, T., Praplan, A. P., Riccobono, F., Rissanen, M. P., Rondo, L.,
910   Schnitzhofer, R., Schobesberger, S., Smith, J. N., Steiner, G., Stozhkov, Y., Tomé, A., Tröstl,
911   J., Tsagkogeorgas, G., Wagner, P. E., Wimmer, D., Ye, P., Baltensperger, U., Carslaw, K.,
912   Kulmala, M., and Curtius, J.: Experimental particle formation rates spanning tropospheric
913   sulfuric acid and ammonia abundances, ion production rates and temperatures, *J. Geophys.
914   Res.-Atmos.*, 121, 12377–12400, doi: 10.1002/2015JD023908, 2016.

916   Kürten, A., Li, C., Bianchi, F., Curtius, J., Dias, A., Donahue, N. M., Duplissy, J., Flagan, R.
917   C., Hakala, J., Jokinen, T., Kirkby, J., Kulmala, M., Laaksonen, A., Lehtipalo, K., Makhmutov,
918   V., Onnela, A., Rissanen, M. P., Simon, M., Sipilä, M., Stozhkov, Y., Tröstl, J., Ye, P., and
919   McMurry, P. H.: New particle formation in the sulfuric acid–dimethylamine–water system:
920   reevaluation of CLOUD chamber measurements and comparison to an aerosol nucleation and
921   growth model, *Atmos. Chem. Phys.*, 18, 845–863, doi: 10.5194/acp-18-845-2018, 2018.

923   Kurtén, T., Torpo, L., Ding, C.-G., Vehkamäki, H., Sundberg, M. R., Laasonen, K., and
924   Kulmala, M.: A density functional study on water-sulfuric acid-ammonia clusters and
925   implications for atmospheric cluster formation, *J. Geophys. Res-Atmos.*, 112, D04210, doi:
926   10.1029/2006JD007391, 2007.

928   Lee, S.-H., Reeves, J. M., Wilson, J. C., Hunton, D. E., Viggiano, A. A., Miller, T. M.,
929   Ballenthin, J. O., and Lait, L. R.: Particle formation by ion nucleation in the upper troposphere
930   and lower stratosphere, *Science*, 301, 1886–1889, doi: 10.1126/science.1087236, 2003.

932   Lehtipalo, K., Rondo, L., Kontkanen, J., Schobesberger, S., Jokinen, T., Sarnela, N., Kürten,
933   A., Ehrhart, S., Franchin, A., Nieminen, T., Riccobono, F., Sipilä, M., Yli-Juuti, T., Duplissy,
934   J., Adamov, A., Ahlm, L., Almeida, J., Amorim, A., Bianchi, F., Breitenlechner, M., Dommen,
935   J., Downard, A. J., Dunne, E. M., Flagan, R. C., Guida, R., Hakala, J., Hansel, A., Jud, W.,
936   Kangasluoma, J., Kerminen, V.-M., Keskinen, H., Kim, J., Kirkby, J., Kupc, A., Kupiainen-
937   Määttä, O., Laaksonen, A., Lawler, M. J., Leiminger, M., Mathot, S., Olenius, T., Ortega, I. K.,
938   Onnela, A., Petäjä, T., Praplan, A., Rissanen, M. P., Ruuskanen, T., Santos, F. D., Schallhart,
939   S., Schnitzhofer, R., Simon, M., Smith, J. N., Tröstl, J., Tsagkogeorgas, G., Tomé, A.,
940   Vaattovaara, P., Vehkamäki, H., Vrtala, A. E., Wagner, P. E., Williamson, C., Wimmer, D.,
941   Winkler, P. M., Virtanen, A., Donahue, N. M., Carslaw, K. S., Baltensperger, U., Riipinen, I.,
942   Curtius, J., Worsnop, D. R., and Kulmala, M.: The effect of acid–base clustering and ions on
943   the growth of atmospheric nano-particles, *Nat. Commun.*, 7, 11594, doi:
944   10.1038/ncomms11594, 2016.

Atmospheric
Chemistry
and Physics
Discussions

945

946 Lehtipalo, K., Yan, C., Dada, L., Bianchi, F., Xiao, M., Wagner, R., Stolzenburg, D., Ahonen,
947 L. R., Amorim, A., Baccarini, A., Bauer, P. S., Baumgartner, B., Bergen, A., Bernhammer, A.-
948 K., Breitenlechner, M., Brilke, S., Buchholz, A., Mazon, S. B., Chen, D., Chen, X., Dias, A.,
949 Dommen, J., Draper, D. C., Duplissy, J., Ehn, M., Finkenzeller, H., Fischer, L., Frege, C.,
950 Fuchs, C., Garmash, O., Gordon, H., Hakala, J., He, X., Heikkinen, L., Heinritzi, M., Helm, J.
951 C., Hofbauer, V., Hoyle, C. R., Jokinen, T., Kangasluoma, J., Kerminen, V.-M., Kim, C.,
952 Kirkby, J., Kontkanen, J., Kürten, A., Lawler, M. J., Mai, H., Mathot, S., Mauldin III, R. L.,
953 Molteni, U., Nichman, L., Nie, W., Nieminen, T., Ojdanic, A., Onnela, A., Passananti, M.,
954 Petäjä, T., Piel, F., Pospisilova, V., Quéléver, L. L. J., Rissanen, M. P., Rose, C., Sarnela, N.,
955 Schallhart, S., Schuchmann, S., Sengupta, K., Simon, M., Sipilä, M., Tauber, C., Tomé, A.,
956 Tröstl, J., Väisänen, O., Vogel, A. L., Volkamer, R., Wagner, A. C., Wang, M., Weitz, L.,
957 Wimmer, D., Ye, P., Ylisirniö, A., Zha, Q., Carslaw, K. S., Curtius, J., Donahue, N. M., Flagan,
958 R. C., Hansel, A., Riipinen, I., Virtanen, A., Winkler, P. M., Baltensperger, U., Kulmala, M.,
959 and Worsnop, D. R.: Multicomponent new particle formation from sulfuric acid, ammonia, and
960 biogenic vapors, *Sci. Adv.*, 12, doi: 10.1126/sciadv.aau5363, 2018.

961

962 Li, C., and McMurry, P. H.: Errors in nanoparticle growth rates inferred from measurements in
963 chemically reacting aerosol systems, *Atmos. Chem. Phys.*, 18, 8979–8993,
964 https://doi.org/10.5194/acp-18-8979-2018, 2018.

965

966 McGrath, M. J., Olenius, T., Ortega, I. K., Loukonen, V., Paasonen, P., Kurtén, T., Kulmala,
967 M., and Vehkamäki, H.: Atmospheric Cluster Dynamics Code: a flexible method for solution
968 of the birth-death equations, *Atmos. Chem. Phys.*, 12, 2345–2355, doi: 10.5194/acp-12-2345-
969 2012, 2012.

970

971 McMurry, P. H.: Photochemical Aerosol Formation from SO_2: A theoretical analysis of smog
972 chamber data, *J. Colloid Interf. Sci.*, 78, 513–527, doi: 10.1016/0021-9797(80)90589-5, 1980.

973

974 McMurry, P. H., and Li, C.: The dynamic behavior of nucleating aerosols in constant reaction
975 rate systems: Dimensional analysis and generic numerical solutions, *Aerosol Sci. Technol.*, 51,
976 1057–1070, doi: 10.1080/02786826.2017.1331292, 2017.

977

978 Nadykto, A. B., and Yu, F.: Strong hydrogen bonding between atmospheric nucleation
979 precursors and common organics, *Chem. Phys. Lett.*, 435, 14–18, doi:
980 10.1016/j.cplett.2006.12.050, 2007.

981

982 Nieminen, T., Lehtinen, K. E. J., and Kulmala, M.: Sub-10 nm particle growth by vapor
983 condensation – effects of vapor molecule size and particle thermal speed, *Atmos. Chem. Phys.*,
984 10, 9773–9779, doi: 10.5194/acp-10-9773-2010, 2010.

985

986 Nocedal, J., and Wright, S. J.: Numerical Optimization, Second edition, Algorithm 7.2,
987 Springer, 2006.

988

989   Nowak, J. B., Neuman, J. A., Bahreini, R., Brock, C. A., Middlebrook, A. M., Wollny, A. G.,
990   Holloway, J. S., Peischl, J., Ryerson, T. B., and Fehsenfeld, F. C.: Airborne observations of
991   ammonia and ammonium nitrate formation over Houston, Texas, *J. Geophys. Res. Atmos.*, 115,
992   D22304, doi: 10.1029/2010JD014195, 2010.

994   Ortega, I. K., Kupiainen, O., Kurtén, T., Olenius, T., Wilkman, O., McGrath, M. J., Loukonen,
995   V., and Vehkamäki, H.: From quantum chemical formation free energies to evaporation rates,
996   *Atmos. Chem. Phys.*, 12, 225–235, doi: 10.5194/acp-12-225-2012, 2012.

998   Steihaug, T.: The Conjugate Gradient Method and Trust Regions in Large Scale Optimization,
999   *Society for Industrial and Applied Mathematics*, 20, 626–637, 1983.

1001 Ter Braak, C. J. F.: A Markov Chain Monte Carlo version of the genetic algorithm Differential
1002 Evolution: easy Bayesian computing for real parameter spaces, *Stat. Comput.*, 16, 239–249,
1003 doi: 10.1007/s11222-006-8769-1, 2006.

1005 Ter Braak, C. J. F., and Vrugt, J. A.: Differential Evolution Markov Chain with snooker updater
1006 and fewer chains, *Stat. Comput.*, 18, 435–446, doi: 10.1007/s11222-008-9104-9, 2008.

1008 Yan, C., Dada, L., Rose, C., Jokinen, T., Nie, W., Schobesberger, S., Junninen, H., Lehtipalo,
1009 K., Sarnela, N., Makkonen, U., Garmash, O., Wang, Y., Zha, Q., Paasonen, P., Bianchi, F.,
1010 Sipilä, M., Ehn, M., Petäjä, T., Kerminen, V.-M., Worsnop, D. R., and Kulmala, M.: The role
1011 of H_2SO_4-NH_3 anion clusters in ion-induced aerosol nucleation mechanisms in the boreal forest,
1012 *Atmos. Chem. Phys.*, 18, 13231–13243, doi: 10.5194/acp-18-13231-2018, 2018.

1014 Yu, F., Nadykto, A. B., Herb, J., Luo, G., Nazarenko, K. M., and Uvarova, L. A.: H_2SO_4–H_2O–
1015 NH_3 ternary ion-mediated nucleation (TIMN): kinetic-based model and comparison with
1016 CLOUD measurements, *Atmos. Chem. Phys.*, 18, 17451–17474, doi: 10.5194/acp-18-17451-
1017 2018, 2018.

Table 1: dH and dS values from this study (‡optimization method, *medians from Monte Carlo simulation) and from the literature. dG values at 298 K. [a]Data from Ortega et al. (2012). [b]Data from Hanson et al. (2012). [c]Data from Yu et al. (2017). ◊Value applies for cluster without involvement of water, with different amounts of water molecules this value varies between 11.52 and 12.59 kcal mol^{-1}. ○Value applies for cluster without involvement of water, with different amounts of water molecules this value varies between 5.71 and 8.37 kcal mol^{-1}.

| Reaction	-dH (kcal mol^{-1})	-dS (cal mol^{-1} K^{-1})	-dG (kcal mol^{-1}) at 298 K
$H_2SO_4 + NH_3 \Leftrightarrow (H_2SO_4)_1(NH_3)_1$	16.7‡, 13.2* (16.00)[a] (15.0)[b]	29.8‡, 29.5* (28.14)[a] (21.8)[b]	7.8‡, 4.4* (7.61)[a] (8.5)[b] (7.77)[c]
$(H_2SO_4)_1(NH_3)_1 + H_2SO_4 \Leftrightarrow (H_2SO_4)_2(NH_3)_1$	27.8‡, 28.2* (29.00)[a] (29.0)[b]	43.1‡, 43.0* (42.90)[a] (52.0)[b]	15.0‡, 15.4* (16.22)[a] (13.5)[b] (11.65)[c,◊]
$(H_2SO_4)_2(NH_3)_1 + NH_3 \Leftrightarrow (H_2SO_4)_2(NH_3)_2$	19.3‡, 21.1* (19.46)[a] (19.0)[b]	34.7‡, 34.4* (33.41)[a] (26.8)[b]	9.0‡, 10.8* (9.5)[a] (11.0)[b] (8.75)[c,○]
$(H_2SO_4)_2(NH_3)_1 + H_2SO_4 \Leftrightarrow (H_2SO_4)_3(NH_3)_1$	18.3‡, 20.6* (21.06)[a] (26.0)[b]	37.6‡, 37.4* (36.69)[a] (35.3)[b]	7.1‡, 9.5* (10.13)[a] (12.5)[b] (7.08)[c]
$(H_2SO_4)_2(NH_3)_2 + H_2SO_4 \Leftrightarrow (H_2SO_4)_3(NH_3)_2$	28.1‡, 31.0* (27.63)[a] (30.0)[b]	38.0‡, 38.1* (38.74)[a] (36.9)[b]	16.8‡, 19.6* (16.09)[a] (19.0)[b] (12.17)[c]
$(H_2SO_4)_3(NH_3)_2 + NH_3 \Leftrightarrow (H_2SO_4)_3(NH_3)_3$	25.7‡, 27.2* (25.48)[a] (20.0)[b]	37.6‡, 37.8* (38.07)[a] (28.5)[b]	14.5‡, 15.9* (14.14)[a] (11.5)[b] (7.42)[c]
$(H_2SO_4)_3 + H_2SO_4 \Leftrightarrow (H_2SO_4)_4$	19.7‡, 23.1* (16.78)[a] (23.0)[b]	27.1‡, 26.8* (27.84)[a] (43.9)[b]	11.6‡, 15.1* (8.48)[a] (9.9)[b] (n.a.)[c]
$(H_2SO_4)_3(NH_3)_1 + H_2SO_4 \Leftrightarrow (H_2SO_4)_4(NH_3)_1$	21.8‡, 21.0* (21.34)[a] (24.5)[b]	43.2‡, 43.9* (43.50)[a] (43.6)[b]	8.9‡, 7.9* (8.38)[a] (11.5)[b] (4.16)[c]
$(H_2SO_4)_3(NH_3)_2 + H_2SO_4 \Leftrightarrow (H_2SO_4)_4(NH_3)_2$	22.9‡, 24.2* (23.04)[a] (26.0)[b]	39.6‡, 39.8* (40.15)[a] (36.9)[b]	11.1‡, 12.3* (11.08)[a] (15.0)[b] (7.48)[c]
$(H_2SO_4)_3(NH_3)_3 + H_2SO_4 \Leftrightarrow (H_2SO_4)_4(NH_3)_3$	27.9‡, 31.1* (27.60)[a] (30.0)[b]	41.1‡, 40.7* (41.09)[a] (34.2)[b]	15.7‡, 19.0* (15.36)[a] (19.8)[b] (12.34)[c]
$(H_2SO_4)_4(NH_3)_3 + NH_3 \Leftrightarrow (H_2SO_4)_4(NH_3)_4$	19.2‡, 20.3 (19.18)[a] (21.0)[b]	28.7‡, 29.1* (28.68)[a] (27.8)[b]	10.6‡, 11.6* (10.63)[a] (12.7)[b] (11.34)[c]

1024
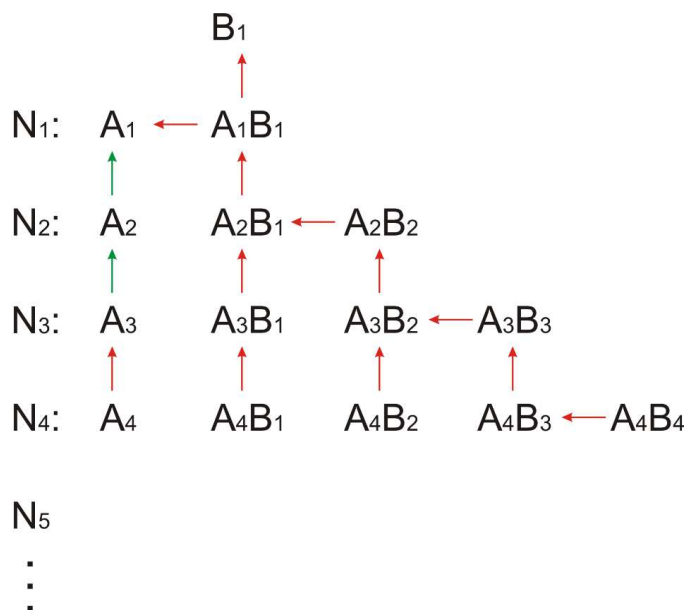
Figure 1. Acid-base scheme implemented in SANTIAGO (Sulfuric acid Ammonia NucleaTIon And GrOwth model). A_xB_y denotes a cluster of sulfuric acid and ammonia with x sulfuric acid molecules and y ammonia molecules. The arrows indicate the considered evaporation rates. Red colors mark the evaporation channels optimized with numeric methods in the present study. Evaporation rates for the channels marked with green arrows were taken from Hanson and Lovejoy (2006). Forward reactions are not shown but the model considers all possible collisions, i.e., cluster-cluster collisions and not just the additions of monomers. Clusters/particles beyond the pentamer (with concentration N_5) are not allowed to evaporate; for these larger clusters, the base content is not considered.

Atmospheric
Chemistry
and Physics
Discussions
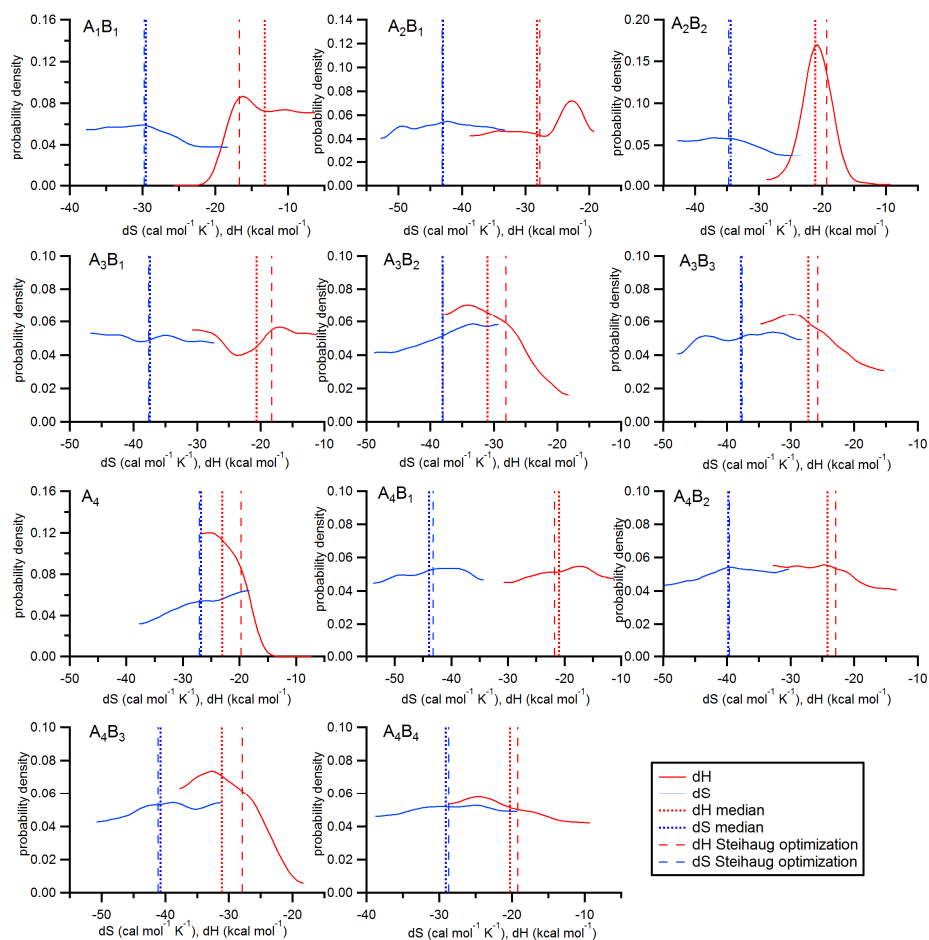
1036
1037
Figure 2: Probability density functions of dH and dS values for 11 clusters in the acid base
system (A$_x$B$_y$ = cluster of sulfuric acid and ammonia with x sulfuric acid molecules and y
ammonia molecules). The vertical lines indicate the values from the optimization method
(dashed lines) and the medians of the probability density functions (dotted lines).
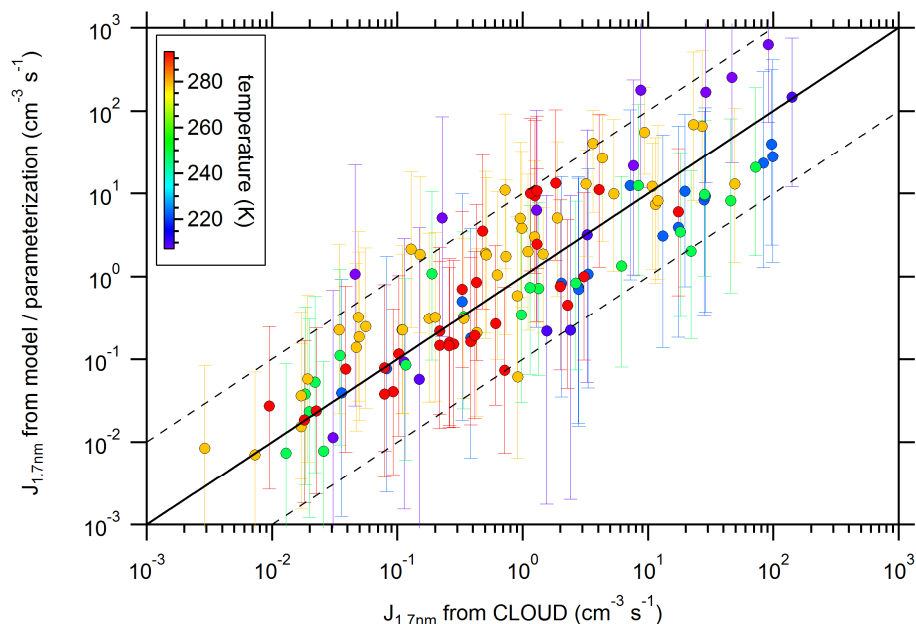
Figure 3: Calculated new particle formation (NPF) rates vs. measured NPF rates (from Kürten et al., 2016). The color code indicates the temperature (between 208 K and 292 K). The calculated values are from the model using the thermodynamic data from Steihaug's optimization method. The solid line indicates the one-to-one correspondence, while the dashed lines indicate a factor of ten deviation from the one-to-one line. The error bars include the uncertainty of the [H_2SO_4] (factor of 2) and the [NH_3] (see Kürten et al., 2016).

Atmospheric
Chemistry
and Physics
Discussions
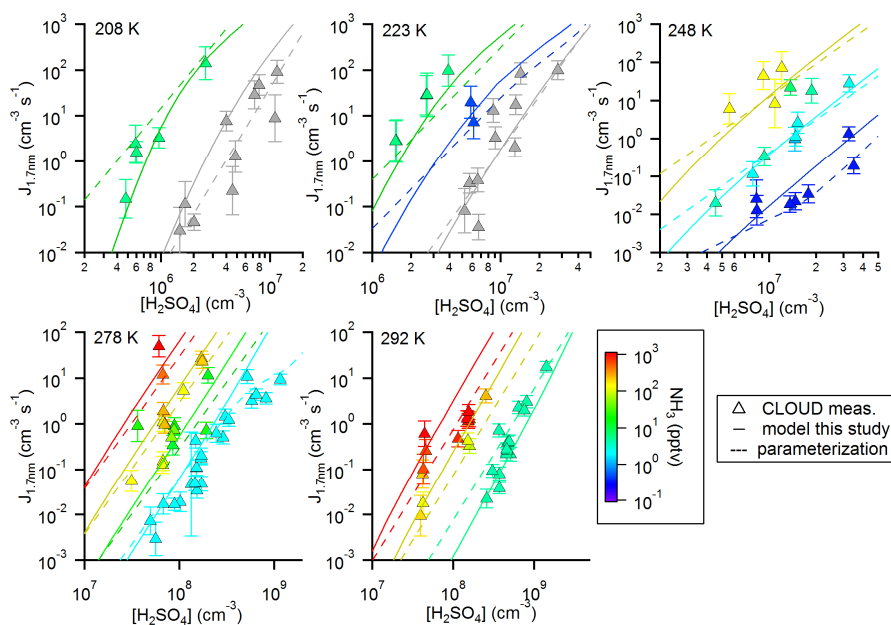

Figure 4: Comparison between simulated and measured new particle formation rates for five different temperatures. The color code indicates the ammonia mixing ratio; the grey symbols indicate pure binary conditions. The model (solid lines) uses thermodynamic data from the optimization scheme according to Steihaug (1983, Section 2.4). The average ratio for the deviation is ~4. In comparison, the results from the parameterization are also shown (dashed lines, Gordon et al., 2017).
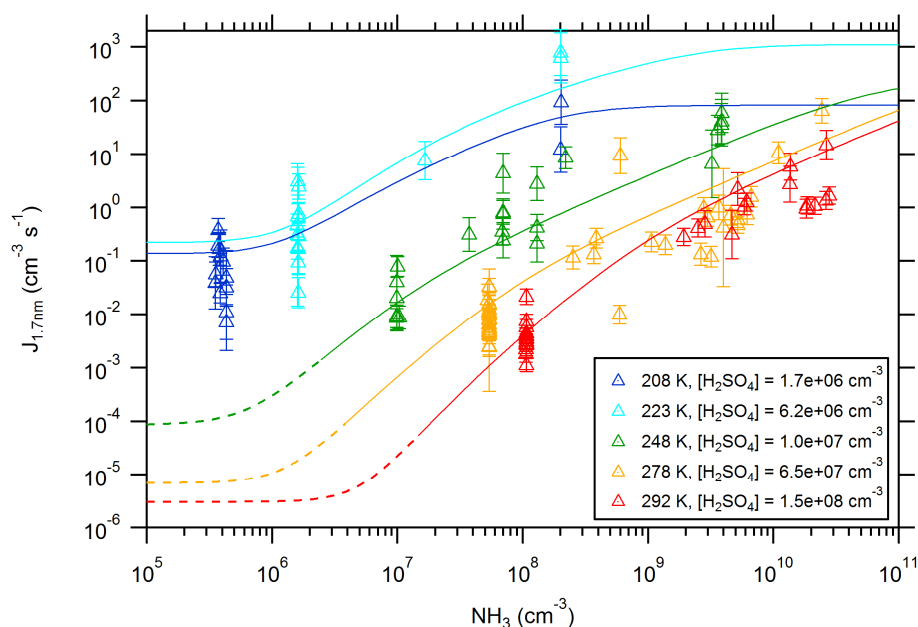
Figure 5: New particle formation rates as a function of the ammonia concentration. The triangles show the neutral formation rates from the CLOUD experiment normalized to the indicated sulfuric acid concentration for five different temperatures (Kürten et al., 2016). The lines show calculated NPF rates from the model using the thermodynamic data from the optimization method (Table 1). The dashed sections (for 248 K, 278 K and 292 K) indicate regions of the parameter space where the model does not give accurate results as the true binary rates are expected to be lower (Ehrhart et al., 2016).

Atmospheric
Chemistry
and Physics
Discussions
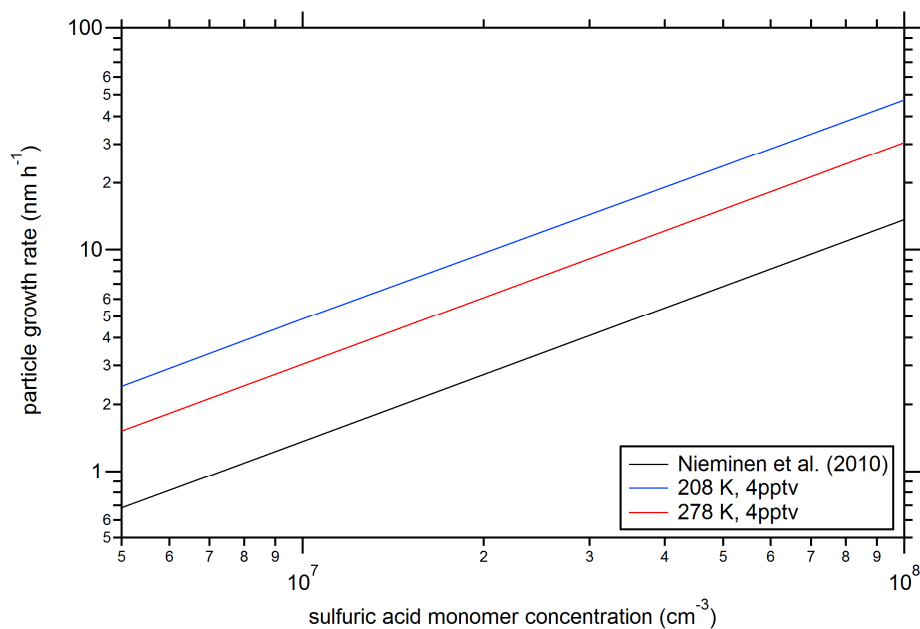
Figure 6: Particle growth rates as a function of the sulfuric acid monomer concentration. The black line indicates the theoretical curve from Nieminen et al. (2010) for a temperature of 278 K and for sulfuric acid vapor. The other lines show the calculated particle growth rates at two different temperatures (indicated in the figure legend).